POLITECNICO DI TORINO
Repository ISTITUZIONALE

New-generation biocompatible Ti-based metallic glass ribbons for flexible implants

Terms of use:

(Article begins on next page)

24 April 2024

New-generation biocompatible Ti-based metallic glass ribbons for flexible implants

Eray Yüce [a,b], Liliana Zarazúa-Villalobos [c], Benoit Ter-Ovanessian [c], Elham Sharifikolouei [d], Ziba Najmi [e], Florian Spieckermann [b,*], Jürgen Eckert [a,b], Baran Sarac [a,*]

[a] Erich Schmid Institute of Materials Science, Austrian Academy of Sciences, Jahnstraße 12, 8700 Leoben, Austria
[b] Department of Materials Science, Montanuniversität Leoben, Jahnstraße 12, 8700 Leoben, Austria
[c] Université de Lyon, INSA-Lyon, UMR CNRS 5510 MATEIS, 20 Avenue Albert Einstein, 69621 Villeurbanne, Cedex, France
[d] Department of Applied Science and Technology, Politecnico di Torino, POLITO, corso duca degli abruzzi 24, 10129 Turin, Italy
[e] Department of Health Sciences, Center for Translational Research on Autoimmune and Allergic Diseases — CAAD, Università Del Piemonte Orientale UPO, Corso Trieste 15/A, 28100 Novara, Italy

HIGHLIGHTS

- Five fully biocompatible Ti-based metallic glasses with different metalloid and soft metal content for a synergistic improvement in corrosion properties.
- For $Ti_{40}Zr_{40}$ bearing alloys the GFA drops due to the low negative enthalpy of mixing between Ti and Zr atoms.
- With increasing Ti and decreasing Zr content, the maximum of the broad diffuse XRD peak shifts to higher 2-Theta angles.
- $Ti_{60}Zr_{20}Si_8Ge_7B_3Sn_2$ and $Ti_{50}Zr_{30}Si_8Ge_7B_3Sn_2$ have a very high pitting potential and wider passivation region compared with other Ti-based MG alloys.

GRAPHICAL ABSTRACT
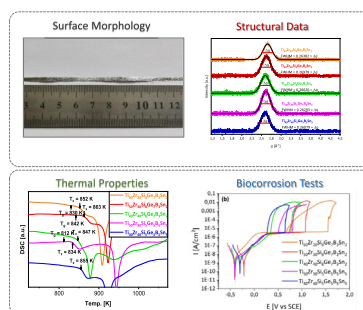
ABSTRACT

We introduce five new biocompatible Ti-based metallic glass (MG) compositions with different metalloid and soft metal content for a synergistic improvement in corrosion properties. Without any potentially harmful elements such as Cu, Ni or Be, these novel alloys can eliminate the risk of inflammatory reaction when utilized for permanent medical implants. Excluding Cu, Ni or Be, which are essential for Ti-based bulk MG production, on the other hand, confines the glass-forming ability of novel alloys to a moderate level. In this study, toxic-element free MG alloys with significant metalloid (Si–Ge–B, 15–18 at.%) and minor soft element (Sn, 2–5 at.%) additions are produced in ribbon form using conventional single-roller melt spinning technique. Their glass-forming abilities and their structural and thermal properties are comparatively investigated using X-ray diffraction (XRD), synchrotron XRD and differential scanning calorimetry. Their corrosion resistance is ascertained in a biological solution to analyze their biocorrosion properties and compare them with other Ti-based bulk MGs along with energy dispersive X-ray. $Ti_{60}Zr_{20}Si_8Ge_7B_3Sn_2$ and $Ti_{50}Zr_{30}Si_8Ge_7B_3Sn_2$ MG ribbons present a higher pitting potential and passivation domain compared with other Ti-based MG alloys tested in similar conditions. Human mesenchymal

* Corresponding authors.
E-mail addresses: florian.spieckermann@unileoben.ac.at (F. Spieckermann), baran.sarac@oeaw.ac.at (B. Sarac).

stem cell metabolic activity and cytocompatibility tests confirm their outstanding cytocompatibility, outperforming Ti-Al6-V4.

1. Introduction

In recent years, titanium (e.g., commercial pure Ti) and its alloys (e.g., Ti–6Al–4 V, Ti–6Al–7Nb, Ti–5Al–2.5Fe) have been the most preferred implant materials for trauma and orthopedic surgery [1,2]. They are widely used for biomedical materials because of their good mechanical properties and reasonable biocompatibility [1,3–7]. However, they have some serious problems yet to be solved, such as unsatisfactory long-term tribology behavior, the release of toxic metallic ions and/or particles through corrosion, stress-shielding effect, and insufficient chemical steadiness in the human body [1,8,9]. Therefore, the development of new titanium alloys with improved biological and biomechanical properties has been a hot research topic for many years [1]. Concurrently, Ti-based bulk metallic glasses (BMGs) have gathered great research interest, and some of them were regarded as potential implant materials owing to their useful engineering properties such as high strength and good corrosion resistance, which are superior to conventional crystalline Ti-alloys [1,10–12]. As a result, a large number of Ti-based BMGs were reported [13]. However, most of these BMGs include Ni and/or Be, which are harmful to the human body because of the well-known cytotoxicity of these elements [14]. It is known that a good glass-forming ability (GFA) usually correlates with systems that exhibit deep eutectics [15]. In these systems, the liquid state is stable down to lower temperatures. When the molten alloy is cooled below the liquidus temperature (T_{liq}), the increasing viscosity hinders the nucleation and growth of crystalline phases, thus promoting the GFA [16]. It is well-known that Cu, Ni and Be present deep eutectics with Ti in their binary phase diagrams [17]. Accordingly, the largest critical diameter of Ti-based BMGs has been reported to be over 50 mm for the $Ti_{32.8}Zr_{30.2}Ni_{5.3}Cu_9Be_{22.7}$ and $Ti_{32.8}Zr_{30.2}Cu_9Fe_{5.3}Be_{22.7}$ systems [18,19].

The first Ti-based BMGs were designed by adding large amounts of Ni and Be to alloy compositions for achieving the highest possible GFA. Nevertheless, the well-known toxicity of these two elements in body fluids has impeded the application of these BMGs as implant materials. In this regard, Ti-based BMGs were proposed for Ti–Zr–Cu-based systems [20]. After the introduction of $Ti_{40}Zr_{10}Cu_{36}Pd_{14}$ BMG with a critical diameter of 6 mm [21,22], many researchers have reported numerous studies on the effects of element additions to this reportedly biocompatible BMG [14,23–28]. Especially upon 2–4 at.% Sn substitution for Cu, cm-sized BMGs were reported by Zhu et al. [25]. In general, these alloys exhibit a combination of outstanding mechanical properties and reasonable corrosion resistance which is superior to that of conventional crystalline Ti-alloys [29]. For instance, $Ti_{40}Zr_{10}Cu_{36}Pd_{14}$ BMG yields a higher strength and lower Young's modulus (2 GPa and 90 GPa, respectively) compared to the crystalline Ti-6Al-4 V alloy (0.97 GPa and 115 GPa, respectively). However, it shows an inferior corrosion resistance in saline solution (0.9 wt.% NaCl) as the pitting corrosion occurs around 500 mV/SCE, while Ti-6Al-4 V alloy exceeds 1.6 V/SCE [29]. The same BMG exhibits similar values (500 mV) in Hanks' solution, whereas Ti-6Al-4 V alloy yields more than 1 V [27]. Further, $Ti_{45}Zr_{10}Cu_{31}Pd_{10}Sn_4$ BMG shows in Hanks' solution about 500 mV/SCE for the pitting initiation [30,31]. The same BMG yields 600 mV/Ag/AgCl in 1 wt.% lactic acid and PBS aqueous solutions [23].

The corrosion resistance is explained by the formation of a protective passive oxide film on the surface of the BMGs [20,22,23].

The existence of this dense passive film, which is mainly composed of TiO_2 and ZrO_2, and also the inherent corrosion resistance of the BMGs due to the absence of internal defects such as grain boundaries and dislocations, has led many authors to refer to these Cu-bearing Ti-based BMGs as biocompatible. As a result, research has concentrated on the improvement of GFA, thermal stability and mechanical properties of these BMGs [20]. Yet, the most important drawback of the $Ti_{40}Zr_{10}Cu_{36}Pd_{14}$ BMG, which is its slight cytotoxicity [32], remains to be solved.

Even though Cu-based shape memory alloys were reported for the potential use in some specific biomedical uses [33,34], it has been regarded for a long time that Cu is a highly cytotoxic element, and its presence should be completely avoided in biocompatible materials designed for long-term implant applications [1,5,6,8,15,31,32]. This rises from the fact that Cu introduces a risk of inflammatory reactions when released into the body fluid, and even an ion release down to 250 ppm can lead to a cytotoxicity effect [35]. This risk can grow for implants with continuous contact with the body fluid under significant load. Harmful Cu ion release was also observed for $Ti_{40}Zr_{10}Cu_{36}Pd_{14}$ BMG, underlining that the amorphous structure of the alloy cannot overcome the risk [32]. Moreover, Cu-bearing Ti-based BMGs present a pronounced sensitivity to pitting corrosion [1,36,37]. Nevertheless, all the Ti-based BMGs previously reported in the literature contain either Ni, Cu and/or Be. Therefore, it is of utmost importance to find new glass-forming alloys without any toxic elements for the efficient utilization of Ti-based metallic glasses in implant materials.

In this regard, there have been very few reports on truly biocompatible Ti-based MGs, in which all the alloy constituents are specifically chosen from only biocompatible elements [1,38]. In their early publications, Inoue et al. investigated the superconductivity of $Ti_{85-x}Nb_xSi_{15}$ ternary as well as $Ti_{55-x}Nb_{30}M_xSi_{15}$ (M = Mo, Ru, Rh, Pd and Ir) and $Ti_{55}Nb_{30}Si_{15-x}M_x$ (M = B, C and Ge) quaternary systems [39,40]. Later, Oak et al. reported the first fully biocompatible glassy alloys of $Ti_{60}Zr_{10}Ta_{15}Si_{15}$ in $(Ti_xZr_yTa_z)_{85}Si_{15}$ and $Ti_{45}Zr_{10}Pd_{40}Si_5$ in $Ti_{45}Zr_{50-x}Pd_xSi_5$ systems [9,11]. Even though these alloys were presented for the first time as potential biomaterials without any harmful elements, the reason behind the avoidance of Cu on purpose was not mentioned. More recently, besides a new fully biocompatible $Ti_{60}Nb_{15}Zr_{10}Si_{15}$ amorphous alloy, an important list of harmful or toxic alloying additions and the non-problematic vital elements was reported by Calin et al. [1,36,38,41–43]. Shortly after, Lin et al. [8] presented the toxic-element-free $Ti_{42}Zr_{40}Ta_3Si_{15}$ amorphous alloy from their study of the $(Ti_xZr_yTa_z)_{85}Si_{15}$ system [3,8,37,44]. It can be stated that all of these compositions except the $Ti_{45}Zr_{10}Pd_{40}Si_5$ amorphous alloy [11] can be traced back to the Ti-Si binary system. The most recently reported truly biocompatible alloys by Calin et al. [45], $Ti_{20}Zr_{20}Nb_{20}Hf_{20}Si_{20}$ and $Ti_{30}Zr_{25}Nb_{25}Si_{15}Ga_3B_2$ are also Ti-based MG alloys, but their design is based on a high entropy alloys (HEA) approach [46], and thus, they feature rather low Ti contents.

It should be underlined that the avoidance of Cu, Ni or Be confines the GFA of biocompatible alloys to a very moderate level. However, we believe there is no possible way to significantly increase the GFA of the Ti-based MGs without using Be, Ni or Cu. Since even the slightest chance of wear release in the body can lead to severe inflammatory reactions [1,35], it is the safest way to exclude these harmful elements from alloy design strategies in the first place. Indeed, this is why all of the "truly biocompatible

[1,38]" Ti-based MGs reported in the literature could only be synthesized in the ribbon form. Since the first report entitled "Attempt to develop a biocompatible Ti-based amorphous alloy" by Oak and Inoue in 2007 [9], the situation has not changed. As mentioned before, these three elements lower T_{liq} of Ti-based alloys drastically [47], and this allows for the use of conventional BMG production methods such as suction or injection casting, which realize rather low critical cooling rates (10^2-10^3 K/s) that are nevertheless sufficient to impede the crystallization of the molten bulk glass-forming alloys [15]. Yet, none of these non-problematic vital elements [1,38] yields such an important reduction in T_{liq} as Cu, Ni, or Be [17] does. This necessitates the need for other quenching methods with much higher cooling rates (10^5-10^6 K/s) like melt-spinning in order to achieve an amorphous structure [15]. Moreover, this confinement brings some additional experimental difficulties to the quenching process. One has to use a crucible (Al_2O_3 or graphite), in which the melting event takes place prior to ejection of the molten alloy, always reacting with Ti, as Ti becomes increasingly reactive at elevated temperatures [48]. In other words, C or O contamination becomes inevitable, and this reduces the GFA of the alloys through increased susceptibility to heterogeneous nucleation. Furthermore, the selection of non-problematic elements allows only metalloids (except very expensive Pd) as the main glass-forming alloy constituents since they possess the largest negative mixing enthalpies as well as the largest atomic size mismatches with the main alloy constituents, that is, Ti and Zr. However, their utilization simultaneously increases the amount of non-directional covalent bonds in the atomic structure, and this accounts for undesired brittleness [15]. Besides, these metalloids usually exhibit positive mixing enthalpies with each other ($\Delta H_{(Ge-B)}^{mix} = 11.48$ kJ/mol, $\Delta H_{(Si-B)}^{mix} = 3.26$ kJ/mol, $\Delta H_{(Si-Ge)}^{mix} = 2.31$ kJ/mol) as well as with some of the vital metallic elements ($\Delta H_{(Sn-B)}^{mix} = 17.78$ kJ/mol, $\Delta H_{(Sn-Si)}^{mix} = 6.34$ kJ/mol, $\Delta H_{(Ga-B)}^{mix} = 5.58$ kJ/mol) [49]. Therefore, strictly limited element selection has to be carried out with extra caution, considering the above-mentioned negative effects on GFA.

To the best of our knowledge, no other toxic-element-free amorphous alloy compositions, which consist of only biocompatible elements (as suggested by Calin et al. [1] and references therein), have been reported until today. In this work, we aim to develop new biocompatible Ti-based metallic glasses with excellent corrosion resistance and evaluate their GFA, selecting alloy compositions based on the Ti-Zr-Si-Ge pseudo-binary system as a starting point. The studied alloys are designed using the empirical rules proposed by Inoue [50], under the classification of TM-M type (Transition Metal - Metalloid) metallic glasses. In this context, we present five new toxic element-free Ti-based MG compositions, namely $Ti_{60}Zr_{20}Si_8Ge_7B_3Sn_2$, $Ti_{50}Zr_{30}Si_8Ge_7B_3Sn_2$, $Ti_{50}Zr_{30}Si_5Ge_5B_5Sn_5$, $Ti_{40}Zr_{40}Si_8Ge_7B_3Sn_2$ and $Ti_{40}Zr_{40}Si_5Ge_5B_5Sn_5$, which can be fabricated in the form of glassy ribbons.

Each phase diagram of the Ti-Si, Ti-Ge, Zr-Si and Zr-Ge binary systems exhibits a deep eutectic reaction at 13.7 at.% Si, 14.9 at.% Ge, 8.8 at.% Si and 9.5 at.% Ge, respectively [17]. As the previously reported fully biocompatible alloys, our glass-forming compositions are also based on metal-metalloid type systems. These alloys generally consist of 75–85 at.% transition metals and 15–25 at.% metalloids [15]. Even though the reason is still not very clear, it is trivial that all of the metal-metalloid type glass-forming alloys require at least 15 at.% metalloid atoms (of one type or a mixture of different metalloids) in order to stabilize the glassy structure, and they commonly feature a deep eutectic around a composition of 15–25 at.% metalloid [15].

In this sense, except in an early study by Inoue et al. [40], silicon has always been the sole metalloid element for metal-metalloid type Ti-based glassy alloys. Besides being very cheap, it is a β-Ti

(BCC) stabilizer, has limited solubility in Ti and the eutectic temperature lies at 1603 K, which is the lowest among the other Ti-metalloid binary systems. Regarding the well-known empirical rules suggested by Inoue [15], it is expected that Si promotes the vitrification of a glass-forming alloy. It yields a large negative heat of mixing value ($\Delta H_{(Ti-Si)}^{mix} = -60.9$ kJ/mol, $\Delta H_{(Zr-Si)}^{mix} = -78.9$ kJ/mol) with the main alloy constituents and a large atomic size mismatch with the Ti atoms [1]. Indeed, Si has been the only reported binary glass-forming (20 at.% Si) metalloid with Ti [51].

Germanium is, on the other hand, an expensive element. Therefore, despite being the same group element as Si, it has never been utilized as the main metalloid glass-former for Ti-based alloys, but only as partial replacements for Si in $Ti_{67.5}Fe_{25}Si_{7.5}$ and $Ti_{55}Nb_{30}Si_{15}$ systems. It has been reported that up to 4 at.% Ge substitution for 15 at.% Si results in an amorphous structure in Ti-Nb-Si alloys [40]. For the Ti-Fe-Si ternary system, the addition of Ge yields a more detrimental effect on the GFA, and vitrification is feasible only up to 1.5 at.% Ge [16]. However, the Ti-Fe-Si ternary system is not biocompatible due to the existence of Fe, and thus, this result can be neglected. Moreover, Ge features a significant atomic size difference with Ti and Zr (both more than 12%) and a large negative mixing enthalpy ($\Delta H_{(Ti-Ge)}^{mix} = -51.3$ kJ/mol and $\Delta H_{(Zr-Ge)}^{mix} = -72.5$ kJ/mol) with the main alloy constituents [1]. Therefore, in spite of its high price and the slightly positive mixing enthalpy with Si [49], we have decided to explore its function as a main metalloid addition.

The participation of boron in biocompatible glass-forming alloys also needs to be further investigated. There is only one study on the addition of B to Ti-based non-toxic glass-forming alloys [40]. It was mentioned that for the $Ti_{55}Nb_{30}Si_{15}$ ternary system, the formation of a single amorphous phase is feasible up to 7 at.% B replacement for Si. Other than that, this element was only used for micro-alloying purposes in Ni- and Cu-bearing Ti-based BMGs [13]. Boron features a much larger atomic size difference with Ti than Si and Ge [1], but its eutectic temperature of 1813 K is the highest [17]. Despite its shallow eutectic point, we have chosen boron as one of the main metalloid elements considering its large negative heat of mixing ($\Delta H_{(Ti-B)}^{mix} = -58$ kJ/mol, $\Delta H_{(Zr-B)}^{mix} = -79.7$ kJ/mol) and substantial atomic size difference with Ti and Zr.

Besides being biocompatible, Zr is chosen as the main alloy constituent due to its larger atomic size than Ti [52]. Moreover, its participation in the formation of the passive film is also important for Ti-based alloys [20,53]. Zr belongs to the same group in the periodic table as Ti, and it decreases the liquidus temperature (T_{liq}) linearly when it is alloyed up to 40 at.% [17]. Thus, even though the heat of mixing for the Ti-Zr at equiatomic composition is only -0.222 kJ/mol [49], its alloying seems indispensable for Ti-metalloid-based glass-forming systems. However, it is worth mentioning that the ternary eutectic composition of $Ti_{78}Zr_{11}Si_{11}$ was reported to be not vitrifiable at all, and even a modified $Ti_{75}Zr_{10}Si_{15}$ alloy was only partially amorphous [1]. There are also some old reports regarding the Ti-Zr-Si ternary system, but none of them features any kind of single amorphous phase formation [54,55].

As anticipated, the selection of a fifth alloying element is also limited by its biological safety. Since Ta and Nb have been studied in detail before, we have excluded these two elements from our alloy designs. More importantly, both Ta and Nb increase T_{liq} significantly when alloyed with Ti [17]. A high T_{liq} makes the quenching process even more challenging since Ti-based alloys become very aggressive at elevated temperatures, and they tend to react with common crucible materials like quartz or graphite [48]. In this sense, we have considered Sn a suitable element since it is one of the few biocompatible and cheap metal candidates that do

not increase the T_{liq} of the alloy and feature a substantial atomic size difference with Ti. Moreover, it was reported to be beneficial to the GFA of the $Ti_{40}Zr_{10}Cu_{36}Pd_{14}$ BMG as Cu substituting alloying addition [25]. Nevertheless, Sn exhibits positive mixing enthalpies with B, Si and Ge (17 kJ/mol, 6.34 kJ/mol and 0.03 kJ/mol at equiatomic compositions, respectively) [49]. Regarding this serious drawback, we did not exploit its participation and limited its content to a maximum of 5 at.%.

It has been known that the inclusion of different elements has a synergistic impact on the corrosion behavior of different alloy systems. For instance, in nanostructured biocompatible high-entropy alloys with multiple principal elements, the increase in the Ti/Zr ratio within the oxide layer further increases the passivation stability [53]. Moreover, superior degradation performance and good long-term reactivity accounted for the synergistic coordination of Co and Mo bimetals [56]. In terms of metallic glasses, Sarac et al. have reported a pronounced decrease in the corrosion current density, highest passivity, and lowest capacitance by simultaneously adding Ni and Co in Fe-based metallic glass ribbons [57]. Further, outstanding corrosion resistance of $Zr_{40}Ti_{35}Ni_{14}Nb_{11}$ metallic glass compared to stainless steel 316L and commercially pure Titanium were ascribed to the combined effect of chemically and structurally homogeneous amorphous structure and protective passive film [58]. Moreover, the synergistic effect of Pt and Pd in alloys containing both noble metals was demonstrated towards hydrogen oxidation reaction [59]. Finally, the combinatorial influence of minor elements such as Sn, Nb and Ta was revealed by the drop in the passivation current density in Ti-Zr-Pd-Cu based metallic glasses in PBS solution [60].

2. Experimental procedure

Master alloys with nominal compositions (at.%) $Ti_{60}Zr_{20}Si_8Ge_7$-B_3Sn_2, $Ti_{50}Zr_{30}Si_8Ge_7B_3Sn_2$, $Ti_{50}Zr_{30}Si_5Ge_5B_5Sn_5$, $Ti_{40}Zr_{40}Si_8Ge_7B_3$-$Sn_2$ and $Ti_{40}Zr_{40}Si_5Ge_5B_5Sn_5$ were prepared via arc melting elemental Ti (99.99%), Zr (99.95%), Si (99.4%), Ge (99.99%), B (99.4%) and Sn (99.99%) under a Zr-gettered high purity Ar (99.999%) atmosphere. During the preparation, the alloy ingots were flipped and remelted four times for homogenization. All casting trials were done under high purity argon atmosphere after flushing the vacuum chamber of the melt spinner twice with argon and going down to a vacuum level of 3.10^{-6} mbar. The velocity of the copper wheel was kept constant at 31.4 m/s. Ribbons of five different alloy compositions were quenched from the abovementioned master alloys using quartz crucibles.

To confirm the flexibility of the material for the implant applications, we have included a bent ribbon image which is a representative alloy with the best corrosion properties (Fig. S1). The as-spun ribbons were subjected to X-ray diffraction (XRD) analysis to ascertain their amorphous structure. These measurements were performed in reflection configuration (D2 phaser – Bruker) using Co-Kα (λ = 1.78897 Å) radiation. In order to compare the lab source and the synchrotron source data with different wavelengths, the obtained diffraction angles 2θ were converted to the momentum vector q, using $q = 4.\pi.\sin(2\theta/2)/\lambda$, where λ is the X-ray wavelength. A computer-controlled differential scanning calorimeter (DSC) was used to determine the glass transition (T_g) and crystallization (T_x) temperatures of the amorphous ribbons. The tests were conducted using a Netzsch DSC 404 F1 Pegasus device under high purity (99.999%) Ar atmosphere at constant heating and cooling rates of 20 K/min.

The corrosion behavior of the different ribbons was analyzed by electrochemical tests in a naturally aerated solution of NaCl at 0.9 wt.%, with an adjusted pH = 7.4 ± 0.1 at room temperature. The solution and temperature were selected as recommended in the ISO 10,271 standard for dentistry applications. The electrochemical measurements were performed in a three-electrode glass cell using a reference 600 potentiostat (Gamry Instruments, USA), a saturated calomel electrode (SCE) as a reference electrode, and a graphite electrode as a counter electrode. Part of the ribbons was immersed as a working electrode. The immersed surface was delimited by a blocking varnish as well as the electrical connection was isolated from the solution. The exact exposed surface was determined a posteriori by optical micrography ($0.1-0.5$ cm^2). The open circuit potential (OCP) was monitored during 7200 s to achieve stationarity of the interface between the working electrode and electrolyte. Subsequently, cyclic polarization tests (CPT) with a scan rate of 1 mV/s starting from −0.2 V vs OCP were conducted. The limit conditions for the forward scan were +2.5 V vs SCE or a current density of 2 mA/cm^2. The reverse scan rate was 1 mV/s, and it was stopped when the current density reached negative values. At least three tests for each composition were performed. After the CPT, the samples were cleaned with ethanol to eliminate the salts. The ribbon's surface and chemical composition were analyzed by scanning electron microscopy (SEM) using a voltage of 10 kV in a TESCAN VEGA 3 microscope coupled with Energy dispersive X-ray spectrometry (EDX). The information was processed with the software AZtec (OXFORD INSTRUMENTS).

In-situ X-ray diffraction was performed on beamline ID 13 using the Extremely Brilliant Source (EBS) of the European Synchrotron Radiation Facility (ESRF) using a Dectris Eiger 4 M detector with a photon energy of 13.0 keV in transmission setup. The beam size amounted to 30 µm, and the sample to detector distance of 0.1091 m. The diffraction patterns were carefully calibrated using an Al_2O_3 reference (NIST 674a), and the pyFAI software [61] was used for azimuthal integration. Full azimuthal integration was used in order to collect the integral geometric information about the sample. The software pyFAI was used for this operation. The usage of the EBS (Extremely Brilliant Source) that is available after the recent upgrade of the ESRF provides unprecedented brilliance. As a focused beam was used, the high photon flux was fully available for the collection of high-quality diffraction patterns with excellent statistics for the diffraction volume.

The cytocompatibility analysis was conducted by Human bone marrow-derived stem cells (hMSC). hMSC were purchased from Merck (PromoCell C-12974) and were cultivated in low-glucose Dulbecco's Modified Eagle Medium (DMEM, Sigma-Aldrich) supplemented with 15% fetal bovine serum (FBS, Merck) and 1% antibiotics (penicillin/streptomycin, Merck) at 37C, 5% CO_2 atmosphere. Cells were cultivated until 80%−90% confluence, detached by a trypsin-ethylene diamine tetra acetic acid (EDTA) solution (0.25% in phosphate buffer saline (PBS), from Merck), harvested and used for experiments. Cells were directly seeded onto specimens' surface at a defined density (5000 cells/sample), and after 4 h of allowing adhesion, 500 µl of culture media was added to each sample. Subsequently, they were cultivated for 24 and 48 h; at each time point, the viability of the cells was evaluated using metabolic activity using the resazurin metabolic assay (alamarBlue™, ready-to-use solution from Life Technologies) by directly adding the dye solution (0.015% in PBS) onto the cell-seeded specimens. After 4 h of incubation in the dark, the fluorescent signals (expressed as relative fluorescent units – RFU) were detected at fluorescence excitation wavelength 570 nm and fluorescence emission reading of 590 nm by spectrophotometer (Spark, Tecan Trading AG, Basel, CH). Moreover, the fluorescent Live/Dead assay was applied to visually check for viable cells (Live/Dead, Viability/Cytotoxicity Kit for mammalian cells, Invitrogen) with a digital EVOS FLoid microscope (from Life Technologies). Finally, Scanning Electron Microscopy (SEM, JSM-IT500, JEOL) imaging was used to compare bacterial attachment on the sample's surface.

3. Results and discussion

3.1. Thermal properties

Fig. 1 (a) displays the continuous-heating DSC scans of the as-spun amorphous ribbons. The $Si_8Ge_7B_3Sn_2$-containing alloys crystallize in a narrower temperature interval, whereas the last two alloys with $Si_5Ge_5B_5Sn_5$ present a distinctly separated two-stage crystallization process. Interestingly, except for the $Ti_{60}Zr_{20}Si_8Ge_7B_3Sn_2$ alloy, the largest crystallization peaks follow a clear trend. When the content of other alloy constituents is equal, that means $Si_8Ge_7B_3Sn_2$ and $Si_5Ge_5B_5Sn_5$ groups, the positions of the main exothermic peaks depend on the Ti-Zr ratio of the alloys. For $Ti_{50}Zr_{30}$-bearing alloys, the main peaks are located at higher temperatures, while $Ti_{40}Zr_{40}$ peaks appear at lower temperatures. However, this trend does not hold for the onset temperatures (T_x) of the smaller exothermic peaks. Even though T_x (=863 ± 2 K) of the $Ti_{50}Zr_{30}Si_8Ge_7B_3Sn_2$ alloy is higher than T_x (=847 ± 2 K) of the $Ti_{40}Zr_{40}Si_8Ge_7B_3Sn_2$ alloy, which is similar to the correlation between their larger peaks, the $Ti_{50}Zr_{30}Si_5Ge_5B_5Sn_5$ alloy exhibits a much lower T_x (=834 ± 2 K) than the T_x (=855 ± 2 K) of the $Ti_{40}Zr_{40}Si_5Ge_5B_5Sn_5$ alloy. Moreover, the $Ti_{50}Zr_{30}Si_5Ge_5B_5Sn_5$ alloy presents the widest temperature interval for the crystallization event.

It is well-known that a precise determination of the glass transition temperature (T_g) can often be problematic for melt-spun metallic glass ribbons [15]. Indeed, for the fully biocompatible Ti-based amorphous alloys, many authors have reported the absence of a clear endothermic event that could account for T_g [1,9,11,45]. Except for the $Ti_{50}Zr_{30}Si_5Ge_5B_5Sn_5$ alloy, this is also the case in this study. Thus, we have subtracted the second heating curves from the initial ones to detect the glass transition event more clearly. Fig. 2. (b) shows the obtained T_g and T_x values of the studied alloys. It can be seen that even after the curve subtraction, the $Ti_{40}Zr_{40}Si_8Ge_7B_3Sn_2$ and $Ti_{40}Zr_{40}Si_5Ge_5B_5Sn_5$ alloys do not reveal a detectable T_g. On the other hand, $Ti_{60}Zr_{20}Si_8Ge_7B_3Sn_2$, $Ti_{50}Zr_{30}Si_8Ge_7B_3Sn_2$, and $Ti_{50}Zr_{30}Si_5Ge_5B_5Sn_5$ exhibit small endothermic bumps just before their crystallization initiate. According to these T_g values, the extension of the supercooled liquid region (SCLR = $\Delta T_x = T_x - T_g$) of the related alloys is calculated, and these values are shown in Table 1.

Table 1 shows that the $Ti_{60}Zr_{20}Si_8Ge_7B_3Sn_2$ and $Ti_{50}Zr_{30}Si_5Ge_5B_5Sn_5$ alloys exhibit a slightly larger ΔT_x than $Ti_{50}Zr_{30}Si_8Ge_7B_3Sn_2$. Besides, $Ti_{50}Zr_{30}Si_5Ge_5B_5Sn_5$ is the only alloy with a distinct T_g, which can be detected from its initial DSC scan without any curve subtraction. Nevertheless, differences between the deduced SCLR

values lie within the error limit of our DSC device, and thus, they cannot be used for a dependable GFA comparison. Another particularly important thermal parameter for GFA, the reduced glass transition temperature ($T_{rg} = T_g/T_{liq}$) of the alloys, cannot be calculated due to the very noisy melting signals of the alloys. This stems from the inevitable reaction between the molten alloy and the Al_2O_3 crucible of the DSC. Considering these drawbacks, we believe that the quality of amorphous samples that could be produced from a single master alloy might play a role in GFA evaluation. It is critical to note that the $Ti_{50}Zr_{30}Si_5Ge_5B_5Sn_5$ alloy has given the most decent ribbons, and all the melt-spinning trials were successful in terms of amorphization. Based on our visual observations, $Ti_{50}Zr_{30}Si_5Ge_5B_5Sn_5$ seems to have a better GFA than the other compositions. During the melt-spinning process, we have tried to find the optimum overheating temperature that yields the best ribbon shape for each alloy. In this context, the majority of the melt-spinning attempts ended up with amorphous ribbons for the $Ti_{40}Zr_{40}Si_5Ge_5B_5Sn_5$ alloy, likewise for $Ti_{50}Zr_{30}Si_5Ge_5B_5Sn_5$. This was not noticed for the alloys that contain $Si_8Ge_7B_3Sn_2$.

3.2. Structural properties

Fig. 2 shows the XRD patterns of the wheel- and air-side of the as-spun ribbons. The broad diffraction maxima on both sides of the ribbons confirm the amorphous atomic structure of the ribbons. The numbers on the image designate the wheel-side diffraction maxima of the corresponding alloys. It can be seen that, for the $Si_8Ge_7B_3Sn_2$ group, the maximum of the broad diffuse maximum shifts to higher 2-theta angles with increasing Ti- and decreasing Zr-content. Since the position of the diffraction maximum is inversely related to the average radius of the first coordination shell [62,63], it can be stated that the first neighbor atomic distance decreases upon Ti replacement for Zr, and the disordered atomic configuration of the alloys becomes denser. This applies to the $Si_5Ge_5B_5Sn_5$ group as well.

Especially for the alloys that contain $Ti_{50}Zr_{30}$, the decrease in average atomic distances is similar for both groups. However, the $Ti_{60}Zr_{20}Si_8Ge_7B_3Sn_2$ alloy exhibits a seemingly denser atomic structure compared to the other alloys, which should be related to the atomic radius of Zr (0.162 nm), the largest of all alloy constituents [52]. Thus, the lowest Zr content should lead to a decrease in average bonding distances, which becomes apparent on the shift of the broad maxima to higher diffraction angles. On the other hand, the average interatomic distance is larger for the $Si_5Ge_5B_5Sn_5$ group at a constant amount of $Ti_{50}Zr_{30}$ and $Ti_{40}Zr_{40}$.
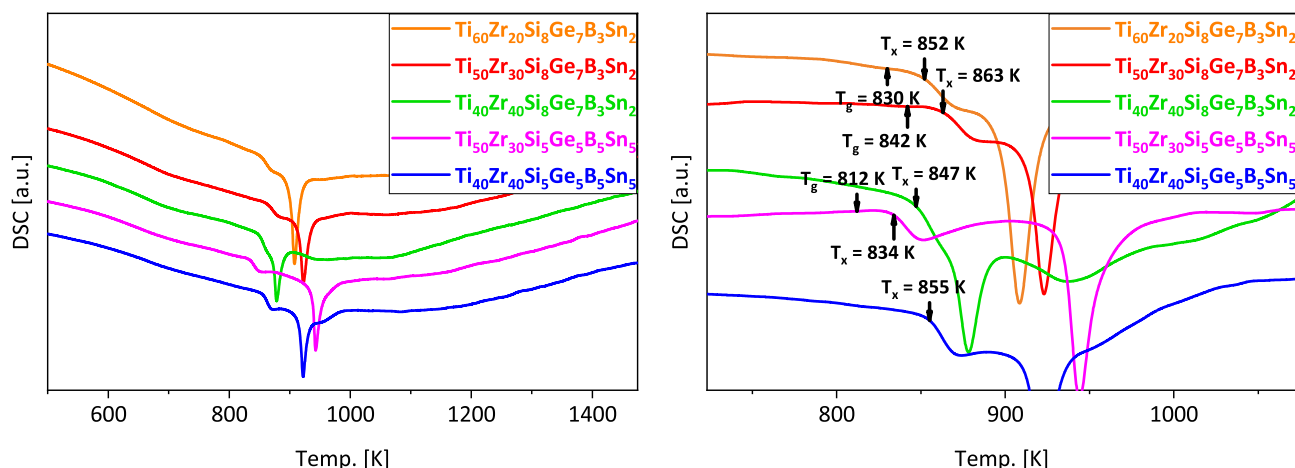

Fig. 1. (a) High-temperature DSC scans of melt-spun glassy ribbons recorded at a heating rate of 20 K/min. **(b)** DSC scans normalized via subtraction of the second heating curve from the first one. The direction of the endothermic events is upwards for both images.
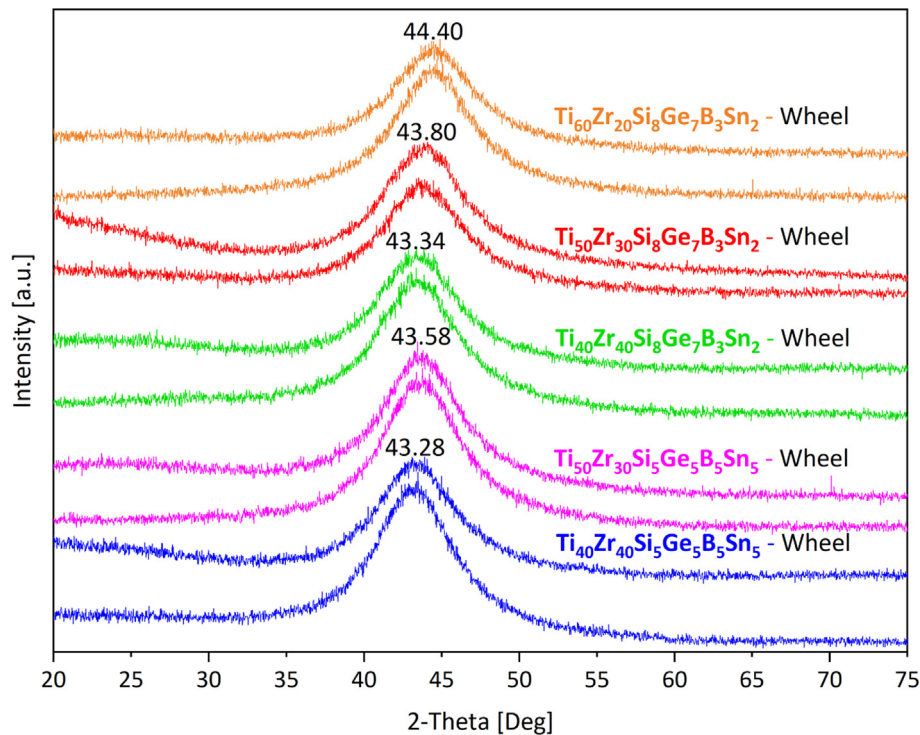
Fig. 2. XRD patterns obtained from the wheel- and air-sides of the as-spun ribbons. The numbers on the image designate the wheel-side diffraction maxima (the curve placed above of the two measurements of the same ribbon type) of the corresponding alloys.

Table 1
Thermal properties ($\Delta T_x = T_x – T_g$, T_g = Glass transition temperature, T_x = Crystallization onset temperature) and ejection temperatures of the investigated alloys. The error limit of the DSC is about ± 2 K.

Alloy	T_g [K]	T_x [K]	$\triangle T_x$ [K]	T_{eject} [K]
$Ti_{60}Zr_{20}Si_8Ge_7B_3Sn_2$	830	852	22	1823
$Ti_{50}Zr_{30}Si_8Ge_7B_3Sn_2$	842	863	21	1893
$Ti_{40}Zr_{40}Si_8Ge_7B_3Sn_2$	–	847	–	1823
$Ti_{50}Zr_{30}Si_5Ge_5B_5Sn_5$	812	834	22	1773
$Ti_{40}Zr_{40}Si_5Ge_5B_5Sn_5$	–	855	–	1883

Recently, a new general relation between the atomic structure and GFA has been proposed by Li et al. [64]. In order to evaluate the GFA of the alloys, the diffraction angle 2θ was converted to the momentum vector q, using $q = 4.\pi.\sin(2\theta/2)/\lambda$, where λ is the X-ray wavelength. They have reported a simple but powerful Δq – GFA correlation for individual ternary alloy libraries, and a large value of the full width at half-maximum (FWHM) of the first broad diffraction maximum, Δq, was proven to be a structural indicator for a high GFA.

In this regard, we have calculated the FWHM values of the studied alloys in order to make a structural GFA comparison. The deduced Δq values of the broad diffraction maxima obtained from conventional XRD scans are depicted in Fig. 3. The values of Δq were obtained via applying a Gaussian nonlinear curve-fitting function to the wheel-side XRD patterns after background subtraction.

According to the ascertained Δq values, the $Ti_{50}Zr_{30}Si_8Ge_7B_3Sn_2$ alloy should possess the highest GFA, whereas $Ti_{50}Zr_{30}Si_5Ge_5B_5Sn_5$ and $Ti_{40}Zr_{40}Si_5Ge_5B_5Sn_5$ should have the worst ones. However, as mentioned before, these two alloys yielded the best results during the melt spinning process. Moreover, the alloys yielding the largest Δq, i.e., $Ti_{50}Zr_{30}Si_8Ge_7B_3Sn_2$ and $Ti_{40}Zr_{40}Si_8Ge_7B_3Sn_2$ ribbons, were the most problematic ones in terms of reproduction. Nevertheless, the general trend of Δq holds also when the values are deduced from the synchrotron XRD patterns.

In Fig. 4, these synchrotron XRD patterns and the applied non-linear curve-fitting function (Voigt) are depicted. It can be seen that, except for the missing $Ti_{60}Zr_{20}Si_8Ge_7B_3Sn_2$ alloy, the order of Δq values is entirely in accordance with the previous ones from Fig. 3. Thus, despite the observed contradiction in reproducibility, it is safe to state that the order of GFA from highest to lowest is as follows: $Ti_{50}Zr_{30}Si_8Ge_7B_3Sn_2$, $Ti_{40}Zr_{40}Si_8Ge_7B_3Sn_2$, $Ti_{50}Zr_{30}Si_5Ge_5B_5Sn_5$ and $Ti_{40}Zr_{40}Si_5Ge_5B_5Sn_5$, excluding $Ti_{60}Zr_{20}Si_8Ge_7B_3Sn_2$.

This result seems especially straightforward considering the positive mixing enthalpies between the minority alloy constituents. In this regard, the most significant enthalpy of mixing values are $\Delta H^{mix}_{(Sn-B)} = 17.78$ kJ/mol, $\Delta H^{mix}_{(Ge-B)} = 11.48$ kJ/mol and $\Delta H^{mix}_{(Sn-Si)} = 6.34$ kJ/mol [49]. However, for the alloys bearing the $Si_5Ge_5B_5Sn_5$ group, this might limit the GFA by violating the third empirical rule of Inoue [50] since there are simply more repelling atomic pairs in their composition compared to the $Si_8Ge_7B_3Sn_2$ bearing alloys. Apparently, B_5Sn_5 affects the GFA more negatively compared with B_3Sn_2, because the number of B-Sn pairs with the largest positive heat of mixing increases significantly.

On the other hand, the GFA of the $Ti_{40}Zr_{40}$ main group appears to be inferior in both alloy pairs. As Zr possesses the largest negative enthalpy of mixing with other minor alloy constituents, at first glance, this seems to contradict the assumptions mentioned above because it is expected that Zr atoms would make stronger bonds with alloying elements than Ti atoms do. As this being true, one also has to take into consideration that $Ti_{40}Zr_{40}$-bearing alloys are quasi-equiatomic compositions, and more importantly, $\Delta H^{mix}_{(Ti-Zr)}$ is only -0.222 kJ/mol at a 0.5-mol fraction of Zr [49]. This emphasizes that when the content of the main constituents equally corresponds to 80 at.% of the alloy, the GFA decreases simply because of the low negative enthalpy of mixing between Ti and Zr atoms. In this regard, one would expect that $Ti_{60}Zr_{20}Si_8Ge_7B_3Sn_2$ should have the highest GFA, considering the fact that the $Ti_{60}Zr_{20}$ group is the farthest from being equiatomic. However, this time
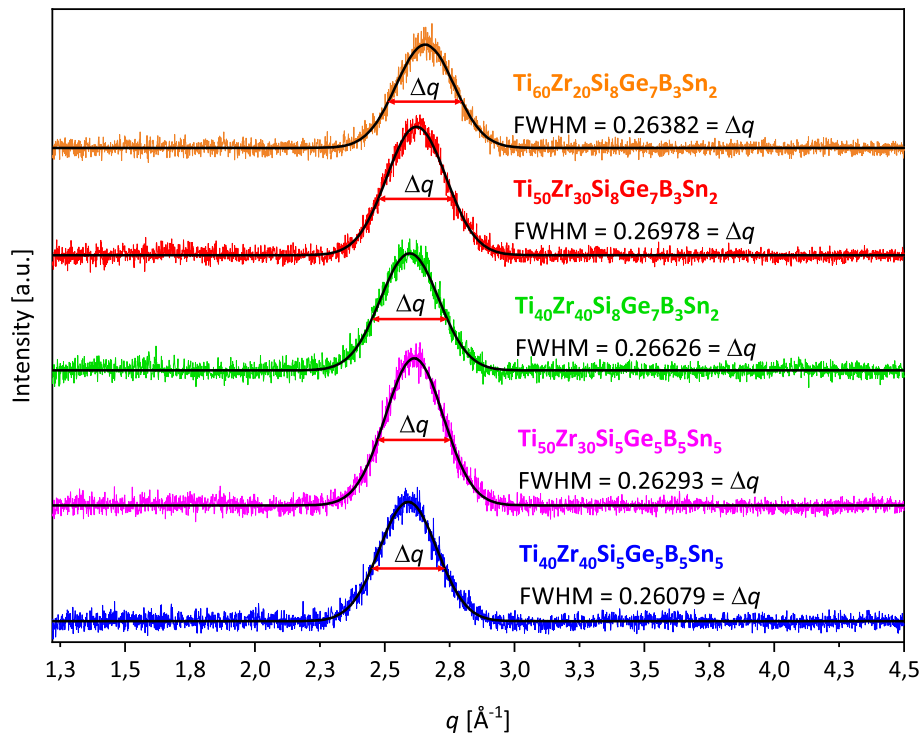
Fig. 3. FWHM (Δq) values of the wheel-side XRD patterns. The Δq values were obtained via applying a Gaussian nonlinear curve-fitting function to the wheel-side XRD patterns after background subtraction.
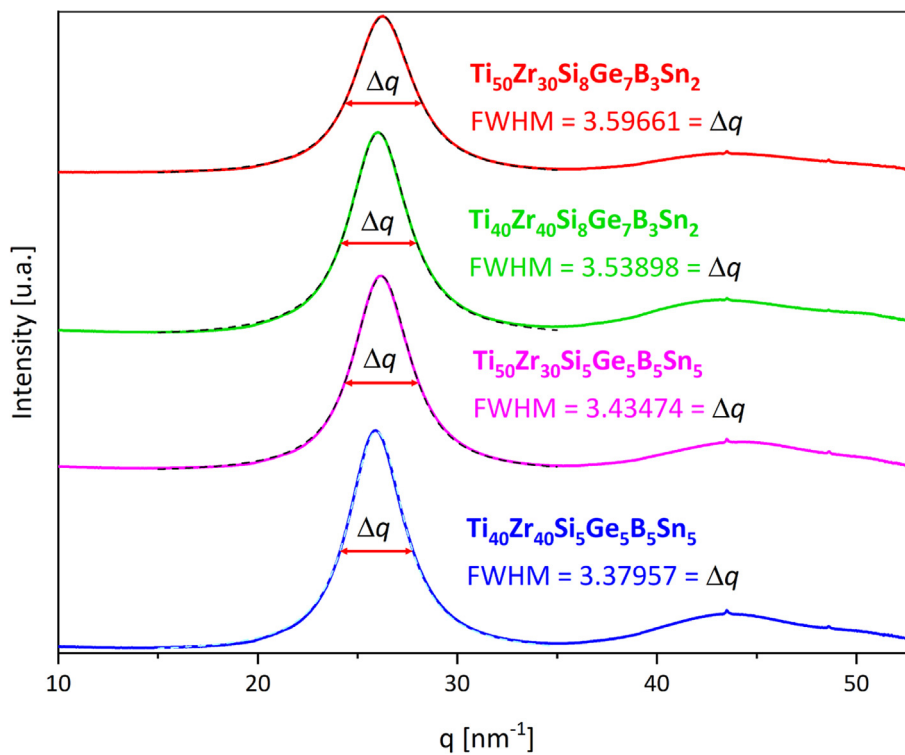

Fig. 4. FWHM (Δq) values obtained from synchrotron XRD patterns. The values of Δq were obtained via applying a nonlinear Voigt function to the synchrotron diffraction peaks of each alloy.

the negative mixing enthalpy of Zr with the other elements plays a decisive role. Zr always yields the largest negative enthalpy of mixing values with the selected alloy elements. For instance, $\Delta H_{(Zr-Si)}^{mix} = -78.4$ kJ/mol, $\Delta H_{(Zr-Ge)}^{mix} = -72.58$ kJ/mol and

$\Delta H_{(Zr-B)}^{mix} = -77.2$ kJ/mol, while $\Delta H_{(Ti-Si)}^{mix} = -60.81$ kJ/mol, $\Delta H_{(Ti-Ge)}^{mix} = -51.33$ kJ/mol and $\Delta H_{(Ti-B)}^{mix} = -65.04$ kJ/mol [49]. Thus, the lower Zr content of Ti$_{60}$Zr$_{20}$Si$_8$Ge$_7$B$_3$Sn$_2$ results in a worse GFA

in comparison to $Ti_{50}Zr_{30}Si_8Ge_7B_3Sn_2$, and this is also confirmed by their Δq values in Fig. 3.

3.3. Potentiodynamic polarization

Representative open-circuit potential (OCP) and the cyclic potentiodynamic polarization curves obtained for each MG tested are shown in Fig. 5. The main electrochemical parameters extracted from these experiments are summarized in Table 2. The OCP curves in Fig. 5(a) show that $Ti_{60}Zr_{20}Si_8Ge_7B_3Sn_2$ and $Ti_{50}Zr_{30}Si_5Ge_5B_5Sn_5$ alloys have a slight increment in the first 3000 sec, indicating passive film formation, and then they reach a relatively steady state. On the other hand, $Ti_{50}Zr_{30}Si_8Ge_7B_3Sn_2$ and $Ti_{40}Zr_{40}Si_5Ge_5B_5Sn_5$ alloys display a steady increase in potential throughout the test period, implying the need for a longer time to stabilize the passive film interface. Finally, $Ti_{40}Zr_{40}Si_8Ge_7B_3Sn_2$ reveals a stable state in the first half of the test, and then the OCP continuously decreases until the end of the test. Similar findings were recorded for $Ti_{50}Zr_{30}Si_8Ge_7B_3Sn_2$ and $Ti_{40}Zr_{40}Si_5Ge_5B_5Sn_5$, but these alloys require more time to stabilize the passive film interface. In all the cases, the OCP reported at the end of the test is within a narrow range from -278 mV to -347 mV (see Table 2), suggesting a comparable passive layer composition and a similar interface. The observed slight differences could be related to the native oxide layer on the ribbons or their surface state.

The cyclic polarization curves in Fig. 5 (b) show the passivation behavior upon anodic polarization for all tested ribbons. The corrosion potential (E_{corr}) appears very close for all the compositions, with differences of less than 100 mV. The passivation current density (I_{pass}) is also very similar, but the passive film grown on $Ti_{50}Zr_{30}Si_5Ge_5B_5Sn_5$ and $Ti_{40}Zr_{40}Si_5Ge_5B_5Sn_5$ seems to achieve a slightly lower current density of 2.4×10^{-6} A/cm^2 followed by the passive state of sample $Ti_{40}Zr_{40}Si_8Ge_7B_3Sn_2$ with $2.58 \pm 0.27 \times 10^{-6}$ A/cm^2. It is worth mentioning that the $Ti_{60}Zr_{20}Si_8Ge_7B_3Sn_2$ alloy shows the highest passivation current density ($2.87 \pm 0.31 \times 10^{-6}$ A/cm^2). The cyclic potentiodynamic technique is also a highly effective method to determine the susceptibility of a metal or alloy to pitting corrosion when exposed to a specific corrosive medium and the probability of repassivation if the passive film is damaged (in the case of passive materials). For this reason, the pitting potential (E_{pit}), the repassivation potential (E_{pp}), and the passivation domain (η_{pit}), which is the difference between E_{pit} and E_{corr}, were measured for all the alloys, and their average values of a minimum of three tests are reported in Table 2.

Conversely to the trends of E_{corr} and I_{pass}, E_{pit}, E_{pp}, and therefore also η_{pit} exhibit significant differences. The alloys $Ti_{60}Zr_{20}Si_8Ge_7B_3Sn_2$ and $Ti_{50}Zr_{30}Si_8Ge_7B_3Sn_2$ have the highest E_{pit} values with

1.48 ± 0.08 V and 1.26 ± 0.18 V vs SCE, followed by $Ti_{40}Zr_{40}Si_8Ge_7B_3Sn_2$ and $Ti_{50}Zr_{30}Si_5Ge_5B_5Sn_5$ amorphous ribbons, which have similar values, 0.73 ± 0.07 V and 0.76 ± 0.04 V vs SCE, respectively. Finally, the $Ti_{40}Zr_{40}Si_5Ge_5B_5Sn_5$ alloy yields the lowest E_{pit} with 0.61 ± 0.08 V vs SCE. The ability of the materials to repassivate after the passive film is damaged, or the repassivation potential (E_{pp}) and η_{pit} follow the same tendency, being headed by the $Ti_{60}Zr_{20}Si_8Ge_7B_3Sn_2$ alloy. Note that the tendencies always favor the alloys with the highest amount of Ti. However, the difference of $E_{pit} - E_{pp}$ is higher in these alloys, e.g., 0.74 ± 0.01 V for the $Ti_{60}Zr_{20}Si_8Ge_7B_3Sn_2$ alloy, suggesting a lower resistance to pit propagation even though it has the widest passivation region and the highest passivation current density. It is also important to mention that, when the pits nucleate, they might perforate the materials and affect the repassivation ability determination.

According to the results, $Ti_{60}Zr_{20}Si_8Ge_7B_3Sn_2$ and $Ti_{50}Zr_{30}Si_8Ge_7B_3Sn_2$ MG ribbons present a high pitting potential (E_{pit}) and passivation region (η_{pit}) in all the cases compared with other Ti-based MG alloys tested in the same or similar conditions [1,8,9,11,30]. For instance, Liens et al. [29] reported $E_{corr} = -0.07$ V, $E_{pit} = 0.5$ V, and $\eta_{pit} = 0.57$ V vs SCE for the $Ti_{40}Zr_{10}Cu_{36}Pd_{14}$ BMG alloy in 0.9 wt% of NaCl at 310 K. Tested under the same conditions Liens et al. [20] reported values of $E_{corr} = -0.016 \pm 0.061$ V, $E_{pit} = 0.365 \pm 0.072$ V, and $\eta_{pit} = 0.381$ V vs SCE for the $Ti_{40}Zr_{10}Cu_{33}Pd_{14}Sn_2$ alloy; and $E_{corr} = -0.016 \pm 0.010$ V vs SCE and $E_{pit} = 0.435 \pm 0.07$ V, and $\eta_{pit} = 0.445$ V vs SCE for the $Ti_{40}Zr_{10}Cu_{34}Pd_{14}Sn_2Si_1$ alloy. Hua et al. [65] reported $E_{corr} = -0.17$ V vs SCE, an $E_{pit} = 0.50$ V, and $\eta_{pit} = 0.67$ V vs SCE for a similar alloy ($Ti_{40}Zr_{10}Cu_{38}Pd_{12}$) tested in phosphate buffer saline solution at room temperature. Although the corrosion potentials are more positive in these alloys, indicating higher stability in the solution [65], the pitting potentials, as well as the passivation region (0.37-0.67 V), are much lower compared with all the alloys reported in this work. The susceptibility of the TiZrCu BMG alloys is linked to the Cu content, so in terms of corrosion, it is beneficial to substitute copper with other elements such as the ones proposed in this work. However, as Cu promotes the glass-forming ability is not always easy to find some substitute. For this reason, $Ti_{60}Zr_{20}Si_8Ge_7B_3Sn_2$ and $Ti_{50}Zr_{30}Si_8Ge_7B_3Sn_2$ compositions are good candidates for biomedical applications thanks to their huge passivation domain and their ability to repassivate.

Fig. 6 (a-d) shows the SEM micrographs of the $Ti_{60}Zr_{20}Si_8Ge_7B_3Sn_2$ and $Ti_{50}Zr_{30}Si_5Ge_5B_5Sn_5$ alloys taken before and after the cyclic polarization. As shown in Fig. 6. (a) and (c), the samples look quite alike in their as-spun state. Since these two alloys exhibit the widest (1.89 V) and the second narrowest (1.12 V) passive region, they represent the relative difference in corrosion resistance accu-
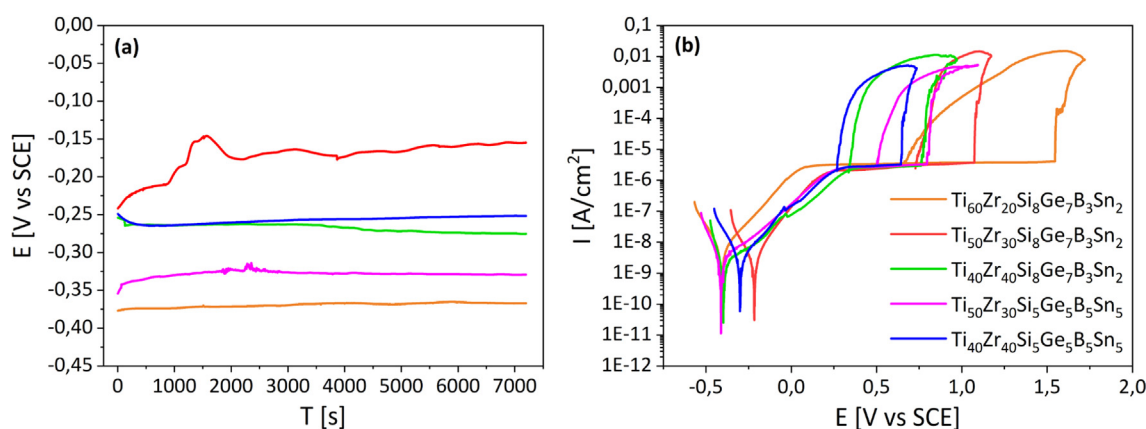

Fig. 5. (a) Open-circuit potential and (b) Cyclic potentiodynamic polarization curves for the Ti-based MG ribbons produced in this work.

Table 2

Electrochemical results for Ti-based alloys with different compositions. OCP = open-circuit potential, E_{corr} = corrosion potential, I_{pass} = passivation current density, E_{pit} = pitting potential, E_{pp} = repassivation potential, $\eta_{pit} = E_{pit} - E_{corr}$ = passivation domain.

Alloy	OCP [V vs SCE]	E_{corr} [V vs SCE]	I_{pass} 10^{-6}[A/cm^2]	E_{pit} [V vs SCE]	E_{pp} [V vs SCE]	η_{pit} [V]	$E_{pit} - E_{pp}$ [V]
$Ti_{60}Zr_{20}Si_8Ge_7B_3Sn_2$	−0.347	−0.378	2.87	1.48	0.73	1.89	0.74
	± 0.02	± 0.04	± 0.31	± 0.08	± 0.08	± 0.12	± 0.01
$Ti_{50}Zr_{30}Si_8Ge_7B_3Sn_2$	−0.288	−0.343	2.81	1.26	0.70	1.60	0.53
	± 0.02	± 0.08	± 0.30	± 0.18	± 0.01	± 0.15	± 0.18
$Ti_{40}Zr_{40}Si_8Ge_7B_3Sn_2$	−0.307	−0.395	2.58	0.73	0.32	1.13	0.41
	± 0.03	± 0.03	± 0.27	± 0.07	± 0.03	± 0.07	± 0.04
$Ti_{50}Zr_{30}Si_5Ge_5B_5Sn_5$	−0.278	−0.356	2.40	0.76	0.49	1.12	0.27
	± 0.05	± 0.05	± 0.27	± 0.04	± 0.01	± 0.08	± 0.03
$Ti_{40}Zr_{40}Si_5Ge_5B_5Sn_5$	−0.289 ± 0.05	−0.333	2.43	0.61	0.28	0.94	0.33
		± 0.04	± 0.37	± 0.08	± 0.04	± 0.11	± 0.07
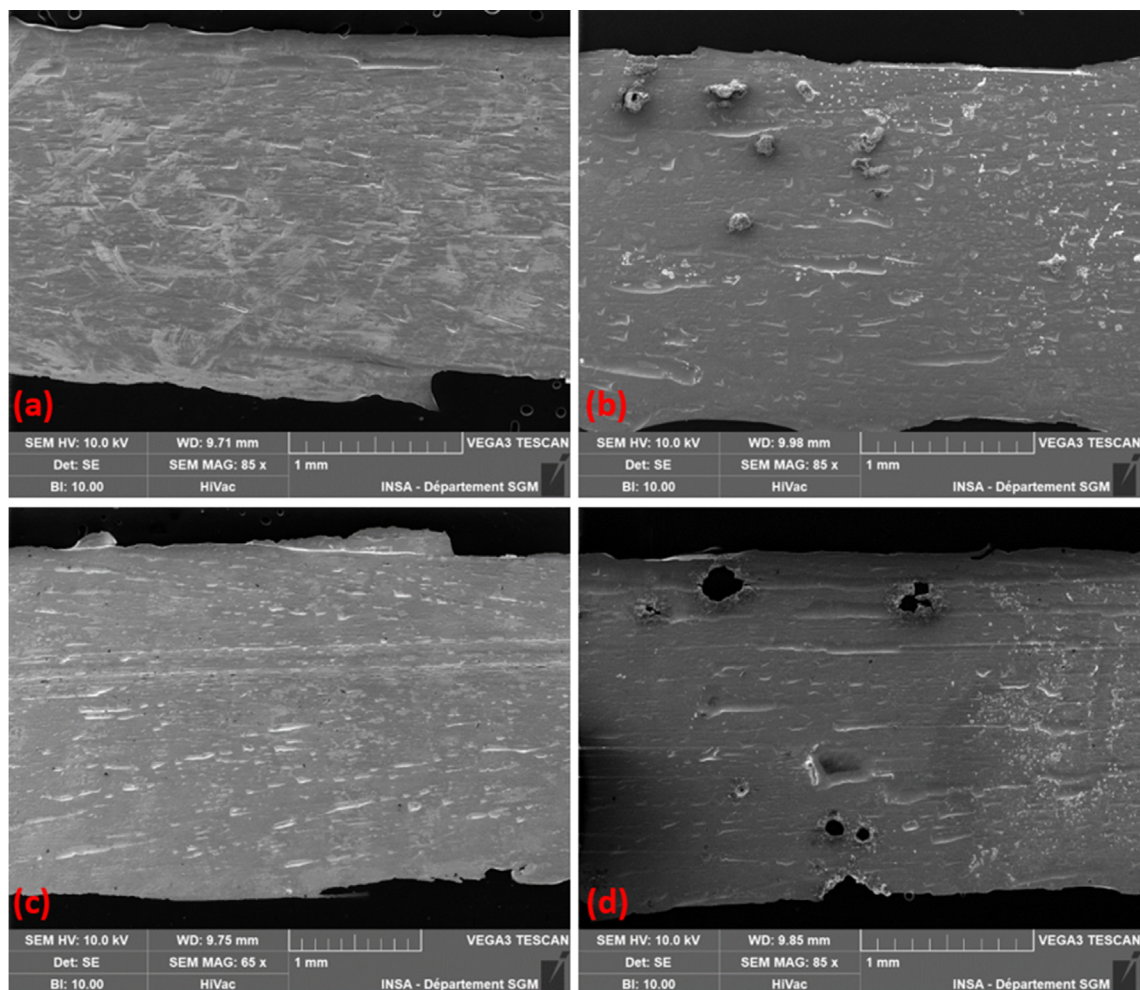
Fig. 6. SEM micrographs of (**a**) as-spun $Ti_{60}Zr_{20}Si_8Ge_7B_3Sn_2$ alloy (**b**) same alloy after the cyclic polarization test (**c**) as-spun $Ti_{50}Zr_{30}Si_5Ge_5B_5Sn_5$ alloy (**d**) same alloy after the cyclic polarization test.

rately. For instance, after reaching a maximum current density of 2 mA/cm^2 during polarization, one can see that $Ti_{50}Zr_{30}Si_5Ge_5B_5Sn_5$ alloy is much more susceptible to NaCl medium and exhibits significant corrosion-related damage, as depicted in Fig. 6. (d). Conversely, the effect of the corrosive environment is not as profound for the $Ti_{60}Zr_{20}Si_8Ge_7B_3Sn_2$ alloy, and although there are some corrosion products on the ribbon surface, no holes are visible, as shown in Fig. 6. (b).

The difference in the integrity of the ribbon's surface is in agreement with the results obtained during the polarization tests, where

the $Ti_{60}Zr_{20}Si_8Ge_7B_3Sn_2$ alloy yields a much better protective passive film compared with the $Ti_{50}Zr_{30}Si_5Ge_5B_5Sn_5$ alloy. This is also the reason why pitting corrosion-related damage observed on the surface of the $Ti_{50}Zr_{30}Si_5Ge_5B_5Sn_5$ ribbon is more pronounced, whereas on the sample $Ti_{60}Zr_{20}Si_8Ge_7B_3Sn_2$ these areas are considerably smaller and the oxides formed are still attached to the surface, which can help to slow down the further pitting growth [66].

To explore the elemental compositions of the pitting corrosion products, these two alloys were subjected to EDX analyses on the designated spots shown in Fig. 7 (a) and (b). The results of the
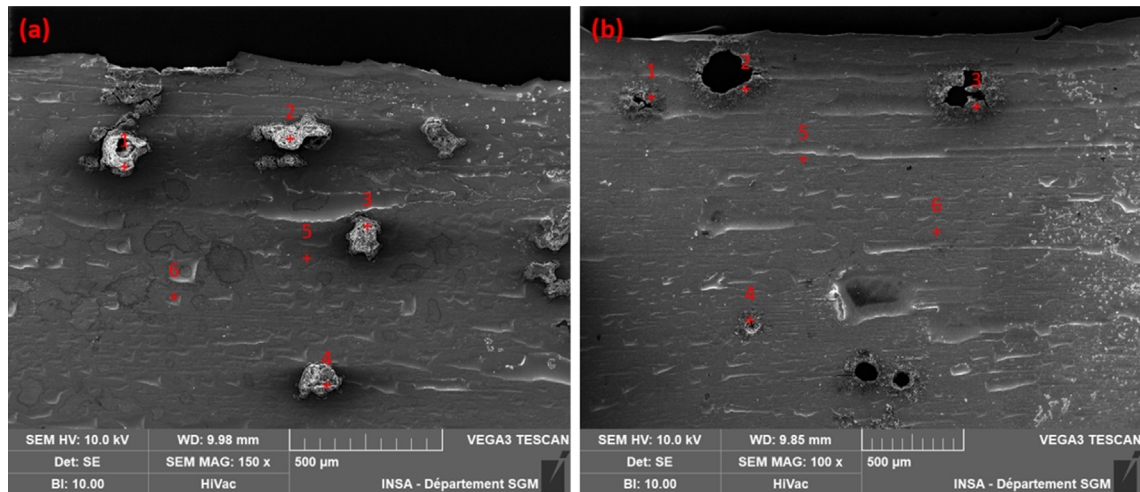
Fig. 7. SEM micrographs used in EDX analysis of the corrosion products of **(a)** $Ti_{60}Zr_{20}Si_8Ge_7B_3Sn_2$ alloy and **(b)** $Ti_{50}Zr_{30}Si_5Ge_5B_5Sn_5$ alloy after the cyclic polarization test. The spots numbered 5 and 6 indicate the alloy surface and used to compare with the corrosion products.

Table 3
EDX analysis of the designated spots shown in Fig. 7. (a) and (b). As-spun sample of $Ti_{60}Zr_{20}Si_8Ge_7B_3Sn_2$ yielded Ti: 55.46, Zr: 20.13, Si: 7.94, Ge: 6.63, Sn:2.28, O: 7.26 in at.%; while as-spun ribbon for $Ti_{50}Zr_{30}Si_5Ge_5B_5Sn_5$ gave out Ti: 49.55, Zr: 26.01, Si:6.59, Ge:4.81, Sn: 4.56, O: 8.48 in at.% (mapped out of the large proportion of the SEM images of the as-spun samples).

Alloy	$Ti_{60}Zr_{20}Si_8Ge_7B_3Sn_2$						$Ti_{50}Zr_{30}Si_5Ge_5B_5Sn_5$					
Spots	**1**	**2**	**3**	**4**	**5**	**6**	**1**	**2**	**3**	**4**	**5**	**6**
Ti	14.82	15.56	17.00	9.29	58.90	55.80	14.20	23.98	34.76	11.95	47.66	49.11
Zr	6.44	5.26	6.03	5.23	19.82	19.09	9.97	13.19	21.22	7.90	29.95	27.47
Si	2.57	2.19	2.63	2.26	5.71	6.17	3.50	4.86	4.21	3.22	4.13	5.11
Ge	2.00	2.60	2.27	2.98	5.06	5.38	1.78	2.29	2.55	2.58	5.81	3.51
Sn	1.10	0.80	0.56	0.51	1.62	1.53	0.50	2.05	4.06	1.11	4.69	5.52
O	73.07	73.59	71.51	79.72	8.89	12.04	70.05	53.53	33.20	73.25	7.77	9.28
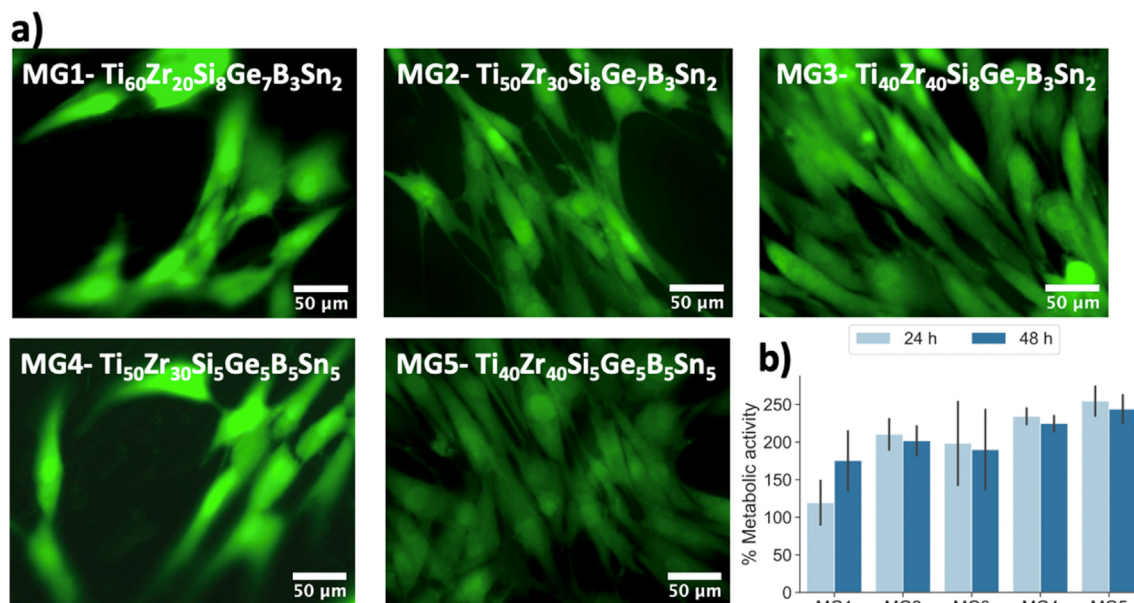
Fig. 8. Cytocompatibility evaluation of metallic glass ribbons: MG1–$Ti_{60}Zr_{20}Si_8Ge_7B_3Sn_2$; MG2–$Ti_{50}Zr_{30}Si_8Ge_7B_3Sn_2$; MG3–$Ti_{40}Zr_{40}Si_8Ge_7B_3Sn_2$; MG4–$Ti_{50}Zr_{30}Si_5Ge_5B_5Sn_5$; MG5–$Ti_{40}Zr_{40}Si_5Ge_5B_5Sn_5$. Human mesenchymal stem cells (hMSC) were cultivated directly on samples surface for 24 and 48 h, and the cytocompatibility was evaluated by: (a) Live/Dead images after 48 h, (b) Metabolic activity after 24 h and 48 h. Ti-6Al-4 V is used as a control sample (100 %).
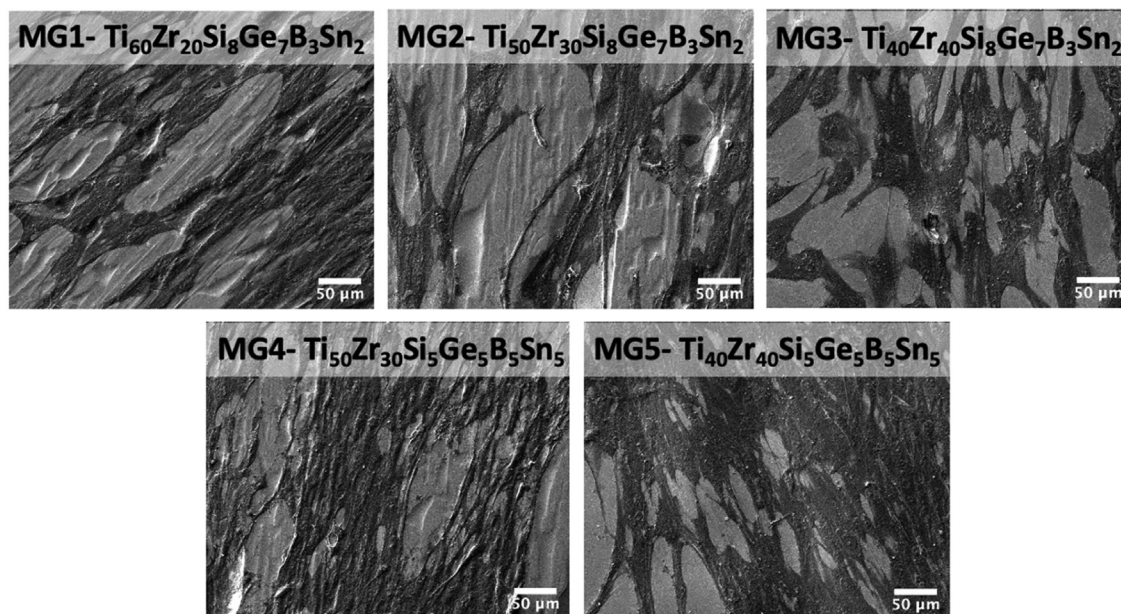
Fig. 9. SEM images of metallic glass ribbons after 48 h cytocompatibility test by human mesenchymal stem cells (hMSC).

related EDX scans are presented in Table 3. Since the detection of B is not possible via EDX, it was excluded from the elemental selection. EDX scans are presented in Table 3. Since the detection of B is not possible via EDX, it was excluded from the elemental selection.

The elemental analysis reveals that points 1, 2, 3 and 4 in both figures stand for corrosion-related oxides, most probably TiO_2 and ZrO_2. This is evident from the significant difference in Ti and Zr contents between these spots and the matrix. Moreover, for both alloys, one can see that the oxygen amount is always higher compared with points 5 and 6. Points 5 and 6 also yield almost the same results as the EDX analysis of the alloys in their as-spun state. Since the pitting corrosion initiates on the local defects or crevices, where the passive oxide layer was penetrated by the corrosive medium, it is expected that spots 5 and 6 yield similar results with as-spun samples.

3.4. Cytocompatibility analysis

Cytocompatibility of metallic glass ribbons was investigated preliminary in vitro on human bone marrow-derived mesenchymal stem cells (hMSC); hMSC cells were directly seeded on the samples' surfaces, and after 24 and 48 h, the viability and the morphology of adhered and spread cells were determined by Live/Dead imaging as reported in Fig. 8 (a), a representative for an 48 h of cultivation. Later, the viability of the cells was further evaluated by employing the metallic activity using the resazurin solution (Alamar blue) assay. Results are reported in Fig. 8 (b), where Ti-6Al-4 V was used as a control sample (%100 Metabolic activity) (Fig. S2).

Further visualization of cells on samples was conducted by SEM and is shown in Fig. 9. According to Fig. 8 and Fig. 9, all metallic glass compositions appear to be fully cytocompatible. Indeed, compared with Ti-6Al-4 V (Fig. S2), they all show considerably better cell viability and metabolic activity. The most cytocompatible metallic glass composition appears to be $Ti_{40}Zr_{40}Si_5Ge_5B_5Sn_5$. In general, $Si_5Ge_5B_5Sn_5$ bearing alloys present better cell viability after 24 h and 48 h.

4. Conclusions

Five new Ti-based MG alloys without any harmful elements have been introduced. As anticipated, the new alloys are marginal

glass formers similar to their truly biocompatible predecessors. A GFA evaluation based on the thermal properties appears ineffective since most alloys do not reveal any T_g. It has been found that the atomic structure of the alloys is quite sensitive to compositional changes. With increasing Ti and decreasing Zr content, the maximum of the broad diffuse XRD peak shifts to higher 2-theta angles, indicating that the first neighbor atomic distance decreases and the disordered atomic configuration of the alloys become denser. $Ti_{60}Zr_{20}Si_8Ge_7B_3Sn_2$ seems to be the densest alloy with the least Zr content.

FWHM values (= Δq) of the amorphous diffraction maxima obtained from conventional and synchrotron XRD experiments reveal that the order of GFA from highest to lowest is $Ti_{50}Zr_{30}Si_8Ge_7B_3Sn_2$, $Ti_{40}Zr_{40}Si_8Ge_7B_3Sn_2$, $Ti_{50}Zr_{30}Si_5Ge_5B_5Sn_5$ and $Ti_{40}Zr_{40}Si_5Ge_5B_5Sn_5$, excluding $Ti_{60}Zr_{20}Si_8Ge_7B_3Sn_2$. Rising from the positive mixing enthalpies between the minority alloy constituents, the alloys bearing the $Si_5Ge_5B_5Sn_5$ group seem to have a lower GFA, since there are more repelling atomic pairs in their composition than the $Si_8Ge_7B_3Sn_2$ group. Apparently, B_5Sn_5 affects the GFA more negatively in comparison to B_3Sn_2-bearing alloys because of the increased number of B-Sn atomic pairs with the largest positive heat of mixing. Moreover, when the content of the main constituents equally corresponds to 80 at.% of the alloy, the GFA drops due to the low negative enthalpy of mixing between Ti and Zr atoms.

Electrochemical tests in a naturally aerated solution of 0.9 wt.% NaCl at room temperature suggests that $Ti_{60}Zr_{20}Si_8Ge_7B_3Sn_2$ and $Ti_{50}Zr_{30}Si_8Ge_7B_3Sn_2$ compositions have a high pitting potential (E_{pit}) and the widest passivation region ($\eta_{pit} = E_{pit} - E_{corr}$) in all the cases compared with other Ti-based MG alloys and Ti-based BMGs tested in the same or similar conditions. The trends are consistent in both alloy groups: The higher the Ti content, the wider the passivation region. On the other hand, the alloys bearing $Si_5Ge_5B_5Sn_5$ yield a clearly inferior corrosion resistance in comparison to their $Si_8Ge_7B_3Sn_2$-bearing counterparts. Apparently, increasing Sn content deteriorates the passivation region. In this sense, structural GFA indicators favor the alloys with higher corrosion resistance. This emphasizes that $Si_5Ge_5B_5Sn_5$-bearing alloys turn out to be less promising than the $Si_8Ge_7B_3Sn_2$-bearing counterparts by means of their GFA and corrosion properties and, thus, B and

Sn coexistence should be avoided for alloy design purposes in the future.

The difference in the corrosion-related damage on the ribbon's surfaces agrees with the results obtained after the cyclic potentiodynamic tests. The pitting damage in the $Ti_{60}Zr_{20}Si_8Ge_7B_3Sn_2$ sample is smaller than in the $Ti_{50}Zr_{30}Si_5Ge_5B_5Sn_5$ sample. The sample of $Ti_{60}Zr_{20}Si_8Ge_7B_3Sn_2$ shows smaller pits with the corrosion products still attached to them (metallic hydroxides), while the sample of $Ti_{50}Zr_{30}Si_5Ge_5B_5Sn_5$ shows larger holes but with no corrosion products. For the characteristics of the pits on the sample $Ti_{60}Zr_{20}Si_8Ge_7B_3Sn_2$, it can be assumed that the pits are in an earlier step of formation due to the most resistant protective passive film formed in this alloy.

Direct cytocompatibility analysis was confirmed for all compositions using human mesenchymal stem cells. The cell metabolic activity on samples' surfaces outperformed the gold standard Ti-Al6-V4 alloy. Further optimization of these Ti-based biocompatible advanced alloys for higher biocorrosion resistance in line with the enhanced glass-forming ability is envisaged by fine-tuning the metalloid and adding appropriate soft metal elements.

Data availability.

The raw/processed data required to reproduce these findings can be provided by the corresponding author upon reasonable request.

CRediT authorship contribution statement

Eray Yüce: Conceptualization, Investigation, Visualization, Formal analysis, Validation, Writing – original draft. **Liliana Zarazúa-Villalobos:** Investigation, Visualization, Formal analysis, Validation, Writing – original draft. **Benoit Ter-Ovanessian:** Supervision, Writing – review & editing. **Elham Sharifikolouei:** Investigation, Visualization, Formal analysis, Validation, Writing – review & editing. **Ziba Najmi:** Investigation, Visualization, Formal analysis, Validation, Writing – review & editing. **Florian Spieckermann:** Investigation, Visualization, Formal analysis, Writing – review & editing. **Jürgen Eckert:** Supervision, Writing – review & editing, Funding acquisition. **Baran Sarac:** Conceptualization, Formal analysis, Validation, Writing – review & editing, Funding acquisition.

Data availability

Data will be made available on request.

Declaration of Competing Interest

The authors declare that they have no known competing financial interests or personal relationships that could have appeared to influence the work reported in this paper.

Appendix A. Supplementary material

Supplementary data to this article can be found online at https://doi.org/10.1016/j.matdes.2022.111139.

References

[1] M. Calin, A. Gebert, A.C. Ghinea, P.F. Gostin, S. Abdi, C. Mickel, J. Eckert, Designing biocompatible Ti-based metallic glasses for implant applications, Mater Sci Eng C Mater Biol Appl 33 (2) (2013) 875–883, https://doi.org/10.1016/j.msec.2012.11.015.

[2] M. Long, H. Rack, Titanium alloys in total joint replacement—a materials science perspective, Biomaterials 19 (18) (1998) 1621–1639, https://doi.org/10.1016/S0142-9612(97)00146-4.

[3] Y.C. Liao, S.M. Song, T.H. Li, J.B. Li, P.H. Tsai, J.S.C. Jang, C.H. Huang, J.C. Huang, Y.S. Huang, C.H. Lin, Y.S. Lin, C.H. Chen, Synthesis and characterization of an open-pore toxic-element-free Ti-based bulk metallic glass foam for bio-implant application, J. Mater. Res. Technol. 9 (3) (2020) 4518–4526, https://doi.org/10.1016/j.jmrt.2020.02.079.

[4] L. Bai, C. Cui, Q. Wang, S. Bu, Y. Qi, Ti–Zr–Fe–Si system amorphous alloys with excellent biocompatibility, J. Non-Cryst. Solids 354 (33) (2008) 3935–3938, https://doi.org/10.1016/j.jnoncrysol.2008.05.015.

[5] S.P. Ong, W.D. Richards, A. Jain, G. Hautier, M. Kocher, S. Cholia, D. Gunter, V.L. Chevrier, K.A. Persson, G. Ceder, Python Materials Genomics (pymatgen): A robust, open-source python library for materials analysis, Comput. Mater. Sci. 68 (2013) 314–319, https://doi.org/10.1016/j.commatsci.2012.10.028.

[6] B. Callegari, J.P. Oliveira, K. Aristizabal, R.S. Coelho, P.P. Brito, L. Wu, N. Schell, F.A. Soldera, F. Mücklich, H.C. Pinto, In-situ synchrotron radiation study of the aging response of Ti-6Al-4V alloy with different starting microstructures, Mater. Charact. 165 (2020) 110400, https://doi.org/10.1016/j.matchar.2020.110400.

[7] B. Callegari, J.P. Oliveira, R.S. Coelho, P.P. Brito, N. Schell, F.A. Soldera, F. Mücklich, M.I. Sadik, J.L. García, H.C. Pinto, New insights into the microstructural evolution of Ti-5Al-5Mo-5V-3Cr alloy during hot working, Mater. Charact. 162 (2020) 110180, https://doi.org/10.1016/j.matchar.2020.110180.

[8] H.C. Lin, P.H. Tsai, J.H. Ke, J.B. Li, J.S.C. Jang, C.H. Huang, J.C. Haung, Designing a toxic-element-free Ti-based amorphous alloy with remarkable supercooled liquid region for biomedical application, Intermetallics 55 (2014) 22–27, https://doi.org/10.1016/j.intermet.2014.07.003.

[9] J.-J. Oak, A. Inoue, Attempt to develop Ti-based amorphous alloys for biomaterials, Mater. Sci. Eng., A 449–451 (2007) 220–224, https://doi.org/10.1016/j.msea.2006.02.307.

[10] J. Schroers, G. Kumar, T.M. Hodges, S. Chan, T.R. Kyriakides, Bulk metallic glasses for biomedical applications, JOM 61 (9) (2009) 21–29, https://doi.org/10.1007/s11837-009-0128-1.

[11] J.-J. Oak, A. Inoue, Formation, mechanical properties and corrosion resistance of Ti–Pd base glassy alloys, J. Non-Cryst. Solids 354 (17) (2008) 1828–1832, https://doi.org/10.1016/j.jnoncrysol.2007.10.025.

[12] A. Rezvan, E. Sharifikolouei, A. Lassnig, V. Soprunyuk, C. Gammer, F. Spieckermann, W. Schranz, Z. Najmi, A. Cochis, A.C. Scalia, L. Rimondini, M. Manfredi, J. Eckert, B. Sarac, Antibacterial activity, cytocompatibility, and thermomechanical stability of $Ti_{40}Zr_{10}Cu_{36}Pd_{14}$ bulk metallic glass, Materials Today Bio 16 (2022) 100378, https://doi.org/10.1016/j.mtbio.2022.100378.

[13] P. Gong, L. Deng, J. Jin, S. Wang, X. Wang, K. Yao, Review on the Research and Development of Ti-Based Bulk Metallic Glasses, Metals 6 (11) (2016) 264, https://doi.org/10.3390/met6110264.

[14] G. Xie, F. Qin, S. Zhu, Recent Progress in Ti-Based Metallic Glasses for Application as Biomaterials, Mater. Trans. 54 (8) (2013) 1314–1323, https://doi.org/10.2320/matertrans.MF201315.

[15] Cia. Suryanarayana, Bulk metallic glasses. [S.l.], CRC Press, 2020.

[16] Y. Guo, I. Bataev, K. Georgarakis, A.M. Jorge, R.P. Nogueira, M. Pons, A.R. Yavari, Ni- and Cu-free Ti-based metallic glasses with potential biomedical application, Intermetallics 63 (2015) 86–96, https://doi.org/10.1016/j.intermet.2015.04.004.

[17] Binary Alloy Phase Diagrams, in: H Okamoto, ME Schlesinger, EM Mueller (Eds.), Alloy Phase Diagrams, ASM International, 2016, p. 89, https://doi.org/10.1002/adma.19910031215.

[18] M.Q. Tang, H.F. Zhang, Z.W. Zhu, H.M. Fu, A.M. Wang, H. Li, Z.Q. Hu, TiZr-base Bulk Metallic Glass with over 50 mm in Diameter, J. Mater. Sci. Technol. 26 (6) (2010) 481–486, https://doi.org/10.1016/S1005-0302(10)60077-1.

[19] L. Zhang, M.Q. Tang, Z.W. Zhu, H.M. Fu, H.W. Zhang, A.M. Wang, H. Li, H.F. Zhang, Z.Q. Hu, Compressive plastic metallic glasses with exceptional glass forming ability in the Ti–Zr–Cu–Fe–Be alloy system, J. Alloy. Compd. 638 (2015) 349–355, https://doi.org/10.1016/j.jallcom.2015.03.120.

[20] A. Liens, B. Ter-Ovanessian, N. Courtois, D. Fabregue, T. Wada, H. Kato, J. Chevalier, Effect of alloying elements on the microstructure and corrosion behavior of TiZr-based bulk metallic glasses, Corros. Sci. 177 (2020) 108854, https://doi.org/10.1016/j.corsci.2020.108854.

[21] S.L. Zhu, X.M. Wang, F.X. Qin, A. Inoue, A new Ti-based bulk glassy alloy with potential for biomedical application, Mater. Sci. Eng., A 459 (1–2) (2007) 233–237, https://doi.org/10.1016/j.msea.2007.01.044.

[22] F. Qin, M. Yoshimura, X. Wang, S. Zhu, A. Kawashima, K. Asami, A. Inoue, Corrosion Behavior of a Ti-Based Bulk Metallic Glass and Its Crystalline Alloys, Mater. Trans. 48 (7) (2007) 1855–1858, https://doi.org/10.2320/matertrans.MJ200713.

[23] J.-J. Oak, D.V. Louzguine-Luzgin, A. Inoue, Fabrication of Ni-free Ti-based bulk-metallic glassy alloy having potential for application as biomaterial, and investigation of its mechanical properties, corrosion, and crystallization

behavior, J. Mater. Res. 22 (5) (2007) 1346–1353, https://doi.org/10.1557/jmr.2007.0154.

[24] S.L. Zhu, X.M. Wang, F.X. Qin, M. Yoshimura, A. Inoue, Effects of Si addition on the glass-forming ability, glass transition and crystallization behaviors of Ti40Zr10Cu36Pd14 bulk glassy alloy, Intermetallics 16 (5) (2008) 609–614, https://doi.org/10.1016/j.intermet.2007.09.012.

[25] S.L. Zhu, X.M. Wang, A. Inoue, Glass-forming ability and mechanical properties of Ti-based bulk glassy alloys with large diameters of up to 1cm, Intermetallics 16 (8) (2008) 1031–1035, https://doi.org/10.1016/j.intermet.2008.05.006.

[26] S. Zhu, G. Xie, F. Qin, X. Wang, A. Inoue, Effect of Minor Sn Additions on the Formation and Properties of TiCuZrPd Bulk Glassy Alloy, Mater. Trans. 53 (3) (2012) 500–503, https://doi.org/10.2320/matertrans.M2011281.

[27] F. Qin, Z. Dan, X. Wang, G. Xie, A. Inoue, Ti-Based Bulk Metallic Glasses for Biomedical Applications, in: A. Laskovski (Ed.), Biomedical Engineering, Trends in Materials Science, InTech, 2011.

[28] F.X. Qin, X.M. Wang, G.Q. Xie, A. Inoue, Distinct plastic strain of Ni-free Ti–Zr–Cu–Pd–Nb bulk metallic glasses with potential for biomedical applications, Intermetallics 16 (8) (2008) 1026–1030, https://doi.org/10.1016/j.intermet.2008.05.004.

[29] A. Liens, A. Etiemble, P. Rivory, S. Balvay, J.-M. Pelletier, S. Cardinal, D. Fabrègue, H. Kato, P. Steyer, T. Munhoz, J. Adrien, N. Courtois, D. Hartmann, J. Chevalier, On the Potential of Bulk Metallic Glasses for Dental Implantology: Case Study on Ti40Zr10Cu36Pd14, Materials (Basel) 11 (2) (2018) 249, https://doi.org/10.3390/ma11020249.

[30] G. Xie, F. Qin, S. Zhu, A. Inoue, Ni-free Ti-based bulk metallic glass with potential for biomedical applications produced by spark plasma sintering, Intermetallics 29 (2012) 99–103, https://doi.org/10.1016/j.intermet.2012.05.006.

[31] G. Xie, H. Kanetaka, H. Kato, F. Qin, W. Wang, Porous Ti-based bulk metallic glass with excellent mechanical properties and good biocompatibility, Intermetallics 105 (2019) 153–162, https://doi.org/10.1016/j.intermet.2018.12.002.

[32] T.H. Li, P.C. Wong, S.F. Chang, P.H. Tsai, J.S.C. Jang, J.C. Huang, Biocompatibility study on Ni-free Ti-based and Zr-based bulk metallic glasses, Mater Sci Eng C Mater Biol Appl 75 (2017) 1–6, https://doi.org/10.1016/j.msec.2017.02.006.

[33] J.P. Oliveira, B. Crispim, Z. Zeng, T. Omori, F.M. Braz Fernandes, R.M. Miranda, Microstructure and mechanical properties of gas tungsten arc welded Cu-Al-Mn shape memory alloy rods, J. Mater. Process. Technol. 271 (2019) 93–100, https://doi.org/10.1016/j.jmatprotec.2019.03.020.

[34] J.P. Oliveira, B. Panton, Z. Zeng, T. Omori, Y. Zhou, R.M. Miranda, F.M. Braz Fernandes, Laser welded superelastic Cu-Al-Mn shape memory alloy wires, Mater. Des. 90 (2016) 122–128, https://doi.org/10.1016/j.matdes.2015.10.125.

[35] A. Reyes-Jara, N. Cordero, J. Aguirre, M. Troncoso, G. Figueroa, Antibacterial Effect of Copper on Microorganisms Isolated from Bovine Mastitis, Front Microbiol 7 (2016) 626, https://doi.org/10.3389/fmicb.2016.00626.

[36] S. Abdi, Investigation of new Ti-based metallic glasses with improved mechanical properties and corrosion resistance for implant applications [Dresden, Technische Universität Dresden, Diss., 2015]. Dresden: Saechsische Landesbibliothek- Staats- und Universitaetsbibliothek Dresden; Technische Universität Dresden; 2015.

[37] M. Nicoara, A. Raduta, R. Parthiban, C. Locovei, J. Eckert, M. Stoica, Low Young's modulus Ti-based porous bulk glassy alloy without cytotoxic elements, Acta Biomater 36 (2016) 323–331, https://doi.org/10.1016/j.actbio.2016.03.020.

[38] S. Bera, P. Ramasamy, D. Şopu, B. Sarac, J. Zálešák, C. Gammer, M. Stoica, M. Calin, J. Eckert, Tuning the glass forming ability and mechanical properties of Ti-based bulk metallic glasses by Ga additions, J. Alloy. Compd. 793 (2019) 552–563, https://doi.org/10.1016/j.jallcom.2019.04.173.

[39] A. Inoue, H.M. Kimura, T. Masumoto, C. Suryanarayana, A. Hoshi, Superconductivity of ductile Ti-Nb-Si amorphous alloys, J. Appl. Phys. 51 (10) (1980) 5475, https://doi.org/10.1063/1.327506.

[40] A. Inoue, T. Masumoto, C. Suryanarayana, A. Hoshi, Superconductivity of ductile titanium-niobium-based amorphous alloys, J. Phys. Colloques 41 (C8) (1980), https://doi.org/10.1051/jphyscol:19808189. C8-758-C8-761.

[41] S. Abdi, M.S. Khoshkhoo, O. Shuleshova, M. Bönisch, M. Calin, L. Schultz, J. Eckert, M.D. Baró, J. Sort, A. Gebert, Effect of Nb addition on microstructure evolution and nanomechanical properties of a glass-forming Ti-Zr-Si alloy, Intermetallics 46 (2014) 156–163, https://doi.org/10.1016/j.intermet.2013.11.010.

[42] S. Abdi, S. Oswald, P.F. Gostin, A. Helth, J. Sort, M.D. Baró, et al., Designing new biocompatible glass-forming Ti75-x Zr10 Nbx Si15 (x = 0, 15) alloys: corrosion, passivity, and apatite formation, J Biomed Mater Res B Appl Biomater 104 (1) (2016) 27–38, https://doi.org/10.1002/jbm.b.33332.

[43] S. Abdi, M. Bönisch, S. Oswald, M.S. Khoshkhoo, W. Gruner, M. Lorenzetti, U. Wolff, M. Calin, J. Eckert, A. Gebert, Thermal oxidation behavior of glass-forming Ti-Zr-(Nb)-Si alloys, J. Mater. Res. 31 (9) (2016) 1264–1274, https://doi.org/10.1557/jmr.2016.122.

[44] M. Nicoara, A. Raduta, C. Locovei, D. Buzdugan, M. Stoica, About thermostability of biocompatible Ti-Zr-Ta-Si amorphous alloys, J Therm

Anal Calorim 127 (1) (2017) 107–113, https://doi.org/10.1007/s10973-016-5532-5.

[45] M. Calin, J. Vishnu, P. Thirathipviwat, M.-M. Popa, M. Krautz, G. Manivasagam, A. Gebert, Tailoring biocompatible Ti-Zr-Nb-Hf-Si metallic glasses based on high-entropy alloys design approach, Mater Sci Eng C Mater Biol Appl 121 (2021) 111733, https://doi.org/10.1016/j.msec.2020.111733.

[46] W.H. Wang, High-Entropy Metallic Glasses, JOM 66 (10) (2014) 2067–2077, https://doi.org/10.1007/s11837-014-1002-3.

[47] H. Okamoto, M.E. Schlesinger, E.M. Mueller, (Eds.). Alloy Phase Diagrams. ASM International; 2016.

[48] S. Fashu, M. Lototskyy, M.W. Davids, L. Pickering, V. Linkov, S. Tai, T. Renheng, X. Fangming, P.V. Fursikov, B.P. Tarasov, A review on crucibles for induction melting of titanium alloys, Mater. Des. 186 (2020) 108295, https://doi.org/10.1016/j.matdes.2019.108295.

[49] A. Debski, R. Debski, W. Gasior, New Features of Entall Database: Comparison of Experimental and Model Formation Enthalpies/ Nowe Funkcje Bazy Danych Entall: Porównanie Doświadczalnych I Modelowych Entalpii Tworzenia, Arch. Metall. Mater. 59 (4) (2014) 1337–1343, https://doi.org/10.2478/amm-2014-0228.

[50] A. Inoue, Stabilization of metallic supercooled liquid and bulk amorphous alloys, Acta Mater. 48 (1) (2000) 279–306, https://doi.org/10.1016/S1359-6454(99)00300-6.

[51] D.E. Polk, A. Calka, B.C. Giessen, The preparation and thermal and mechanical properties of new titanium rich metallic glasses, Acta Metall. 26 (7) (1978) 1097–1103, https://doi.org/10.1016/0001-6160(78)90137-2.

[52] A. Takeuchi, A. Inoue, Classification of Bulk Metallic Glasses by Atomic Size Difference, Heat of Mixing and Period of Constituent Elements and Its Application to Characterization of the Main Alloying Element, Mater. Trans. 46 (12) (2005) 2817–2829, https://doi.org/10.2320/matertrans.46.2817.

[53] B. Sarac, V. Zadorozhnyy, Y.P. Ivanov, F. Spieckermann, S. Klyamkin, E. Berdonosova, M. Serov, S. Kaloshkin, A.L. Greer, A.S. Sarac, J. Eckert, Transition metal-based high entropy alloy microfiber electrodes: Corrosion behavior and hydrogen activity, Corros. Sci. 193 (2021) 109880, https://doi.org/10.1016/j.corsci.2021.109880.

[54] S.H. Whang, Y.Z. Lu, Y.W. Kim, Microstructures and age hardening of rapidly quenched Ti-Zr-Si alloys, J Mater Sci Lett 4 (7) (1985) 883–887, https://doi.org/10.1007/BF00720529.

[55] M. Bulanova, S. Firstov, I. Gornaya, D. Miracle, The melting diagram of the Ti-corner of the Ti-Zr-Si system and mechanical properties of as-cast compositions, J. Alloy. Compd. 384 (1–2) (2004) 106–114, https://doi.org/10.1016/j.jallcom.2004.02.060.

[56] M. Tang, L. Lai, D. Ding, T. Liu, W. Kang, N. Guo, B.o. Song, S. Guo, Rapid degradation of Direct Blue dye by Co-based amorphous alloy wire, J. Non-Cryst. Solids 576 (2022) 121282, https://doi.org/10.1016/j.jnoncrysol.2021.121282.

[57] B. Sarac, Synergistic Effect of Ni and Co Alloying on Corrosion Behavior of Fe (Ni,Co)P13C7 Metallic Glasses in 1M NaCl Solution. Int. J. Electrochem. Sci. 2021:ArticleID:211256. https://doi.org/10.20964/2021.12.55.

[58] M.M. Khan, K.M. Deen, W. Haider, Combinatorial development and assessment of a Zr-based metallic glass for prospective biomedical applications, J. Non-Cryst. Solids 523 (2019), https://doi.org/10.1016/j.jnoncrysol.2019.119544 119544.

[59] V. Hasannaeimi, S. Mukherjee, Noble-Metal based Metallic Glasses as Highly Catalytic Materials for Hydrogen Oxidation Reaction in Fuel Cells, Sci Rep 9 (1) (2019) 12136, https://doi.org/10.1038/s41598-019-48582-7.

[60] J.-J. Oak, D.V. Louzguine-Luzgin, A. Inoue, Investigation of glass-forming ability, deformation and corrosion behavior of Ni-free Ti-based BMG alloys designed for application as dental implants, Mater. Sci. Eng., C 29 (1) (2009) 322–327, https://doi.org/10.1016/j.msec.2008.07.009.

[61] G. Ashiotis, A. Deschildre, Z. Nawaz, J.P. Wright, D. Karkoulis, F.E. Picca, et al., The fast azimuthal integration Python library: pyFAI, J Appl Crystallogr 48 (Pt 2) (2015) 510–519, https://doi.org/10.1107/s1600576715004306.

[62] H.Y. Jung, M. Stoica, S. Yi, D.H. Kim, J. Eckert, Electrical and magnetic properties of Fe-based bulk metallic glass with minor Co and Ni addition, J. Magn. Magn. Mater. 364 (2014) 80–84, https://doi.org/10.1016/j.jmmm.2014.04.028.

[63] F. Wang, A. Inoue, Y. Han, F.L. Kong, S.L. Zhu, E. Shalaan, et al., Excellent soft magnetic Fe-Co-B-based amorphous alloys with extremely high saturation magnetization above 1.85 T and low coercivity below 3 A/m, J. Alloy. Compd. 711 (2017) 132–142, https://doi.org/10.1016/j.jallcom.2017.03.341.

[64] M.-X. Li, Y.-T. Sun, C. Wang, L.-W. Hu, S. Sohn, J. Schroers, W.-H. Wang, Y.-H. Liu, Data-driven discovery of a universal indicator for metallic glass forming ability, Nat Mater 21 (2) (2022) 165–172, https://doi.org/10.1038/s41563-021-01129-6.

[65] N. Hua, X. Hong, L. Lin, Z. Liao, L. Zhang, X. Ye, Q. Wang, Mechanical, corrosion, and wear performances of a biocompatible Ti-based glassy alloy, J. Non-Cryst. Solids 543 (2020) 120116, https://doi.org/10.1016/j.jnoncrysol.2020.120116.

[66] G.S. Frankel, Pitting Corrosion of Metals: A Review of the Critical Factors, J. Electrochem. Soc. 145 (6) (1998) 2186–2198, https://doi.org/10.1149/1.1838615.